

Numerical simulation of anode heat transfer of nitrogen arc utilizing two-temperature chemical non-equilibrium model

Chong Niu(牛冲), Surong Sun(孙素蓉), Jianghong Sun(孙江宏), and Haixing Wang(王海兴)
Citation: Chin. Phys. B, 2021, 30 (**9**): 095206. DOI: 10.1088/1674-1056/ac133a
Journal homepage: http://cpb.iphy.ac.cn; http://iopscience.iop.org/cpb

What follows is a list of articles you may be interested in

Characteristics of DC arcs in a multi-arc generator and their application in the spheroidization of SiO_2

Qifu Lin(林启富), Yanjun Zhao(赵彦君), Wenxue Duan(段文学), Guohua Ni(倪国华), Xingyue Jin(靳兴月), Siyuan Sui(隋思源), Hongbing Xie(谢洪兵), and Yuedong Meng(孟月东)
Chin. Phys. B, 2020, 29 (**12**): 125201. DOI: 10.1088/1674-1056/ab9de9

Experimental study on energy characteristics and ignition performance of recessed multichannel plasma igniter

Bang-Huang Cai(蔡帮煌), Hui-Min Song(宋慧敏), Min Jia(贾敏), Yun Wu(吴云), Wei Cui(崔巍), Sheng-Fang Huang(黄胜方)
Chin. Phys. B, 2020, 29 (**6**): 065207. DOI: 10.1088/1674-1056/ab820c

Characteristics of non-thermal AC arcs in multi-arc generator

Qifu Lin(林启富), Yanjun Zhao(赵彦君), Wenxue Duan(段文学), Guohua Ni(倪国华), Xinyue Jin(靳兴月), Siyuan Sui(隋思源), Hongbing Xie(谢洪兵), Yuedong Meng(孟月东)
Chin. Phys. B, 2019, 28 (**12**): 125205. DOI: 10.1088/1674-1056/ab55ce

Fluctuation of arc plasma in arc plasma torch with multiple cathodes

Zelong Zhang(张泽龙), Cheng Wang(王城), Qiang Sun(孙强), Weidong Xia(夏维东)
Chin. Phys. B, 2019, 28 (**9**): 095201. DOI: 10.1088/1674-1056/ab344b

Experimental investigation on electrical characteristics and ignition performance of multichannel plasma igniter

Sheng-Fang Huang(黄胜方), Hui-Min Song(宋慧敏), Yun Wu(吴云), Min Jia(贾敏), Di Jin(金迪), Zhi-Bo Zhang(张志波), Bing-Xuan Lin(林冰轩)
Chin. Phys. B, 2018, 27 (**3**): 035203. DOI: 10.1088/1674-1056/27/3/035203

Numerical simulation of anode heat transfer of nitrogen arc utilizing two-temperature chemical non-equilibrium model*

Chong Niu(牛冲), Surong Sun(孙素蓉)†, Jianghong Sun(孙江宏), and Haixing Wang(王海兴)‡

School of Astronautics, Beihang University, Beijing 100191, *China*

(Received 22 May 2021; revised manuscript received 4 July 2021; accepted manuscript online 12 July 2021)

A detailed understanding of anode heat transfer is important for the optimization of arc processing technology. In this paper, a two-temperature chemical non-equilibrium model considering the collisionless space charge sheath is developed to investigate the anode heat transfer of nitrogen free-burning arc. The temperature, total heat flux and different heat flux components are analyzed in detail under different arc currents and anode materials. It is found that the arc current can affect the parameter distributions of anode region by changing plasma characteristics in arc column. As the arc current increases from 100 A to 200 A, the total anode heat flux increases, however, the maximum electron condensation heat flux decreases due to the arc expansion. The anode materials have a significant effect on the temperature and heat flux distributions in the anode region. The total heat flux on thoriated tungsten anode is lower than that on copper anode, while the maximum temperature is higher. The power transferred to thoriated tungsten anode, ranked in descending order, is heat flux from heavy-species, electron condensation heat, heat flux from electrons and ion recombination heat. However, the electron condensation heat makes the largest contribution for power transferred to copper anode.

Keywords: nitrogen arc, anode heat transfer, chemical non-equilibrium model, space charge sheath

PACS: 52.80.Mg, 52.40.Hf, 52.65.–y, 52.40.Kh **DOI:** 10.1088/1674-1056/ac133a

1. Introduction

Understanding anode heat transfer is of great significance for the improvement of arc processing performance and extension of arc device lifetime.[1–6] Considerable studies of heat transfer between plasma and anode have been conducted for argon free-burning arc.[7–9] Compared with argon, nitrogen is a shielding gas with good protection, cheap cost and better energy source property, which is usually used in gas tungsten arc welding.[10,11] However, to our knowledge, there are few researches on the anode heat transfer of nitrogen arc both in experiments and numerical simulations.

At present the experimental measurements of nitrogen free-burning arc mainly focus on the temperature distributions and arc voltage characteristics. In Ref. [12], in order to avoid the anode ablation, a tungsten disc with 2% thorium oxide was used as the water-cooling anode to obtain the temperature distribution of nitrogen arc by the spectroscopic technology.[12] The laser-scattering measurement technology was adopted to get the temperature distributions of nitrogen arc without the local thermal equilibrium (LTE) assumption in Ref. [13]. However, it is difficult to accurately measure the anode surface parameters such as temperature and heat flux distributions due to the steep parameters gradient, strong light emission, arc instability, etc. Therefore, the numerical simulation is required to investigate the plasma characteristics of nitrogen arc, especially the anode parameters distributions.

Compared with the numerical modeling of argon and helium arc, there have been few simulations of nitrogen free-burning arc. Most of the existing nitrogen arc models are based on the local thermal equilibrium (LTE) and local chemical equilibrium (LCE) assumptions without complete consideration of the space charge sheath.[10,14] However, the plasma near electrodes obviously deviates from LTE[15–17] and LCE,[18,19] thus the thermal and chemical non-equilibrium model is required to study the anode heat transfer of nitrogen arc. In our previous paper,[20] a thermal and chemical non-equilibrium model has been developed for nitrogen arc, but we did not focus on the anode heat transfer characteristics. Moreover, in the previous studies,[21,22] the space charge sheath can significantly affect the plasma energy flux and species flux on the anode surface. Therefore, the space charge sheath model should be included in the non-equilibrium model to accurately solve the species, current components, heat fluxes, and other parameters on the anode surface.

In this paper, a two-temperature chemical non-equilibrium model, coupled with collisionless space charge sheath model, has been developed for nitrogen arc. The numerical results are first compared with experimental data to validate the numerical model. Then the anode heat transfer of nitrogen arc is investigated utilizing this non-equilibrium model under different input current conditions and different anode materials.

*Project supported by the National Natural Science Foundation of China (Grant Nos. 11735004 and 12005010).

†Corresponding author. E-mail: ssr18@buaa.edu.cn

‡Corresponding author. E-mail: whx@buaa.edu.cn

© 2021 Chinese Physical Society and IOP Publishing Ltd

2. Model description

In this section, the conservation equations and boundary conditions used in the non-equilibrium model are illustrated.

2.1. Assumptions

The calculation domain of the numerical model is shown in Fig. 1. ABCDHG is the flow affected region, ABC is the cathode surface, and EFGH is the anode region. The radius of the cathode tip, i.e., AB is 0.5 mm, and the cone angle of the cathode is 60°. The calculation domain is consistent with the structure of the experimental device in Ref. [12].

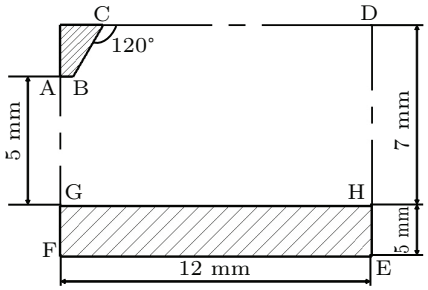


Fig. 1. The computational domain for the numerical model.

The non-equilibrium model is developed on the basis of the following assumptions: (1) the arc is rotationally symmetrical operated with a non-ablating plane anode perpendicular to the arc axis. (2) Only self-induced magnetic field is included in the numerical model, i.e., no external magnetic field. (3) The shielding gas is atmospheric pressure nitrogen and the gas flow is laminar. (4) Radiation loss is considered through net emission coefficient method. (5) Gravity and the effects of viscosity dissipation are negligible. (6) The electron and heavy-species temperatures are assumed in their own Maxwellian distributions. Therefore, the electron and heavy-species energy equations are separately solved, and the energy exchange between electron and heavy-species is based on the elastic collision processes.

2.2. Species and chemical reactions considered

Species considered in this paper include electrons (e), nitrogen molecules (N_2), nitrogen molecular ions (N_2^+), nitrogen atoms (N), monovalent atomic ions (N^+) and divalent atomic ions (N^{++}). Ten forward reactions are described in Table 1 and the corresponding backward reactions are also taken into account in the model. The species and kinetic processes of reactions numbers 1–9 are based on the previous studies of nitrogen thermal plasma.[23–25] Since the maximum temperature can reach 29000 K in our calculation, the divalent atomic ions and reaction process 10 and corresponding reverse process are considered in this paper. The rates of forward reactions numbers 1–9 are given by Arrhenius equation $\alpha_l^{\mathrm{f}} = a_l T^{b_l} \exp(-c_l/T)$, a_l, b_l and c_l are the constants obtained by Dunn and Lordi.[25] The rate of reaction 10 given in Table 1 is obtained from Ref. [26]. Backward reaction rates are obtained by the equilibrium constant method $\alpha_l^{\mathrm{r}} = \alpha_l^{\mathrm{f}} K_l(T)$, where $K_l(T)$ is the equilibrium constant. In Table 1, Ψ_l is the reaction heat.

Table 1. The reactions taken in account in the numerical model.

No.	Reactions	a_l	b_l	c_l	Ψ_l (eV)
1	$N_2+N_2 \leftrightarrow N+N+N_2$	4.98×10^{-9}	–1.5	113260	9.759
2	$N_2+N \leftrightarrow N+N+N$	2.49×10^{-8}	–1.5	113260	9.759
3	$N_2^+ + N \leftrightarrow N_2 + N^+$	1.30×10^{-19}	0.5	0	–1.047
4	$N_2^+ + e \leftrightarrow N+N$	2.49×10^{-8}	–1.5	0	–5.821
5	$N^+ + e + e \leftrightarrow N + e$	2.29×10^{-20}	–4.5	0	–14.534
6	$N_2^+ + N_2 + e \leftrightarrow N_2 + N_2$	6.07×10^{-34}	–2.5	0	–15.580
7	$N_2^+ + N + e \leftrightarrow N_2 + N$	1.66×10^{-35}	–2.5	0	–15.580
8	$N^+ + N_2 + e \leftrightarrow N + N_2$	6.07×10^{-34}	–2.5	0	14.534
9	$N^+ + N + e \leftrightarrow N + N$	1.66×10^{-35}	–2.5	0	–14.534
10	$N^{++} + e + e \leftrightarrow N^+ + e$	$2.2\times10^{-12}\left(\frac{T_e}{10000[\mathrm{K}]}\right)^{-0.639}$			–29.600

2.3. Governing equations

Mass continuity equation

$$\frac{\partial \rho}{\partial t} + \nabla \cdot (\rho \boldsymbol{v}) = 0, \tag{1}$$

where ρ is the mass density and $\boldsymbol{v}$ is the mass-averaged velocity. ρ is calculated by the relation $\rho = \sum_i n_i m_i$, where n_i and m_i are respectively the number density and mass for specie i.

Momentum equation

$$\frac{\partial(\rho \boldsymbol{v})}{\partial t} + (\rho \boldsymbol{v} \cdot \nabla)\boldsymbol{v} = -\nabla p + \nabla \cdot \hat{\tau} + \boldsymbol{j} \times \boldsymbol{B} \tag{2}$$

where p is the gas pressure. $\boldsymbol{j} \times \boldsymbol{B}$ is the Lorentz force, $\boldsymbol{j}$ is the current density and $\boldsymbol{B}$ is the self-induced magnetic field. $\hat{\tau}$ is the viscous stress tensor, expressed for Newtonian flow as follows:

$$\nabla_r \cdot \hat{\tau} = \frac{\partial}{\partial z}\left[\mu\left(\frac{\partial v_r}{\partial z} + \frac{\partial v_z}{\partial r}\right)\right] + \frac{2}{r}\frac{\partial}{\partial r}\left[\mu r\left(\frac{\partial v_r}{\partial r}\right)\right] - 2\mu\frac{v_r}{r^2}, \tag{3}$$

$$\nabla_z \cdot \hat{\tau} = 2\frac{\partial}{\partial z}(\mu\frac{\partial v_z}{\partial z}) + \frac{1}{r}\frac{\partial}{\partial r}\left[\mu r\left(\frac{\partial v_z}{\partial r} + \frac{\partial v_r}{\partial z}\right)\right], \tag{4}$$

where μ is the viscosity of the shielding gas calculated by[27]

$$\mu = \sum_i \frac{X_i \mu_{\mathrm{h}i}}{\sum_j X_j \phi_{ij}}, \tag{5}$$

where X_i is the mole fraction of species i. ϕ_{ij} is a dimensionless quantity calculated by the relation

$$\phi_{ij} = \frac{1}{\sqrt{8}}\left(1+\frac{m_i}{m_j}\right)^{-0.5}\left[1+\left(\frac{\mu_{\mathrm{h}i}}{\mu_{\mathrm{h}j}}\right)^{0.5}\left(\frac{m_j}{m_i}\right)^{0.25}\right]^2.$$

The $\mu_{\mathrm{h}i}$ is the viscosity of species i described as

$$\mu_{\mathrm{h}i} = \frac{5}{16}\frac{\sqrt{\pi m_i k_{\mathrm{B}} T}}{\pi \sigma_i^2 \Omega^{(2,2)^*}}, \tag{6}$$

where k_{B} represents the Boltzmann constant and T is the temperature of the corresponding species. σ_i is the collisional diameter and $\Omega^{(2,2)^*}$ is the collisional integral.[28]

General species equation

$$\frac{\partial \rho_i}{\partial t} + \nabla \cdot (\rho_i \boldsymbol{v}) = -\nabla \cdot \boldsymbol{J}_i + S_i, \tag{7}$$

where $\boldsymbol{J}_i$ is the mass diffusive flux calculated by Eq. (8), S_i is the reaction source term. In Eq. (8), D_i is the effective diffusion coefficient of species i obtained by the relation $D_i = (1-Y_i)/\left(\sum_{j\neq i} X_j/D_{ij}\right)$, $Y_i = n_i m_i/\rho$ is the mass fraction and D_{ij} represents the binary diffusion coefficient[29] calculated by Eq. (9),

$$\boldsymbol{J}_i = -\rho D_i \nabla Y_i, \tag{8}$$

$$D_{ij} = \frac{3}{16}\frac{\sqrt{2\pi k_{\mathrm{B}}^3 T_{ij}^3/m_{ij}}}{p\pi\sigma_{ij}^2\Omega^{(1,1)^*}}, \tag{9}$$

where T_{ij} is the reduced temperature and m_{ij} is the reduced mass for the species i and j. For the ion equations, the ambipolar diffusion coefficient $D_{\mathrm{amb},i}$ instead of D_i is used to calculate the ion diffusive flux.[30]

The densities of N, N_2^+, N^+, and N^{++} are calculated by species conservation equations, the molecular density is solved by the state equation, and the electron density is determined by the quasi-neutrality condition.

Heavy-species energy equation

$$\frac{3}{2}k_{\mathrm{B}}\frac{\partial(n_{\mathrm{h}}T_{\mathrm{h}})}{\partial t} + \nabla\cdot\left(\frac{5}{2}n_{\mathrm{h}}k_{\mathrm{B}}T_{\mathrm{h}}\boldsymbol{v}\right) = \nabla\cdot\left(\lambda_{\mathrm{h}}\nabla T_{\mathrm{h}} - \sum_{i\neq e} h_i \boldsymbol{J}_i\right) + E_{\mathrm{ec}} - \sum_l E_{\mathrm{r},l}^{\mathrm{h}}, \tag{10}$$

where T_{h} is the heavy-species temperature and n_{h} is the total number density of heavy-species. λ_{h} represents the thermal conductivity of heavy-species calculated by Eq. (11) and h_i is the species specific enthalpy. E_{ec} is the energy exchange term between electrons and heavy-species by elastic collision shown in Eq. (12) and $E_{\mathrm{r},l}^{\mathrm{h}}$ is the reaction heat of chemical reaction l expressed in Eq. (13);

$$\lambda_{\mathrm{h}} = \frac{15}{8}\nu_{\mathrm{h,th}}\sum_{i\neq e} n_i l_i, \tag{11}$$

$$E_{\mathrm{ec}} = \sum_{i\neq e}\frac{2m_{\mathrm{e}}}{m_i}\cdot\frac{3}{2}k_{\mathrm{B}}(T_{\mathrm{e}}-T_{\mathrm{h}})n_{\mathrm{e}}n_i\left(\frac{8k_{\mathrm{B}}T_{\mathrm{e}}}{\pi m_{\mathrm{e}}}\right)^{0.5}Q_{ei}, \tag{12}$$

$$E_{\mathrm{r},l}^{\mathrm{h}} = \psi_l\left(\alpha_l^{\mathrm{f}}\prod_{i=1}^{N} n_i^{\beta_{il}^{\mathrm{f}}} - \alpha_l^{\mathrm{r}}\prod_{i=1}^{N} n_i^{\beta_{il}^{\mathrm{r}}}\right). \tag{13}$$

In Eq. (11), l_i is the mean free path of heavy particle i and $\nu_{\mathrm{h,th}}$ is the heavy-species thermal velocity. T_{e} represents the electron temperature solved by Eq. (14) and Q_{ei} is the elastic collision section between the electron and heavy-species. In Eq. (13), β_{il}^{f} and β_{il}^{r} are the stoichiometric numbers of species i in the reaction l for forward reaction and backward reaction, respectively.

Electron energy equation

$$\frac{3}{2}k_{\mathrm{B}}\frac{\partial(n_{\mathrm{e}}T_{\mathrm{e}})}{\partial t} + \nabla\cdot\left(\frac{5}{2}n_{\mathrm{e}}k_{\mathrm{B}}T_{\mathrm{e}}\boldsymbol{v}\right) = \nabla\cdot(\lambda_{\mathrm{e}}\nabla T_{\mathrm{e}} - \boldsymbol{J}_{\mathrm{e}}h_{\mathrm{e}}) + \boldsymbol{j}\cdot\boldsymbol{E} - E_{\mathrm{ec}} - \sum_l E_{\mathrm{r},l}^{\mathrm{e}} - 4\pi\varepsilon, \tag{14}$$

where n_{e} is the electron number density and h_{e} is the electron specific enthalpy. The electron mass diffusive flux $\boldsymbol{J}_{\mathrm{e}}$ is expressed by the relation $\boldsymbol{J}_{\mathrm{e}} = \frac{\boldsymbol{j}}{q_{\mathrm{e}}} - \sum_{i\neq e}\frac{q_i}{q_{\mathrm{e}}}\boldsymbol{J}_i$. q_i is the charge per unit mass of specie i. λ_{e} represents the thermal conductivity of electrons calculated by the formula in Ref. [24]. $-4\pi\varepsilon$ represents the radiation energy loss and ε is the net emission coefficient shown in Ref. [31]. $E_{\mathrm{r},l}^{\mathrm{e}}$ is the reaction heat caused by the electron impact reactions.

Current continuity, Ohm's law, and Maxwell's equation

$$\nabla\cdot\boldsymbol{j} = 0, \tag{15}$$

$$\boldsymbol{j} = -\sigma_{\mathrm{e}}\nabla V, \tag{16}$$

$$\nabla^2\boldsymbol{A} = -\mu_0\boldsymbol{j}. \tag{17}$$

In Eq. (16), the electric conductivity σ_{e} is calculated by $\sigma_{\mathrm{e}} = \frac{e^2 n_{\mathrm{e}}}{m_{\mathrm{e}}\nu_{\mathrm{m}}}$. ν_{m} is the electron collision frequency expressed as the sum of collision frequencies between electrons and heavy-species, and V is the electric potential. In Eq. (17), A is the vector potential, μ_0 is permeability of vacuum, and $\boldsymbol{B} = \nabla\times\boldsymbol{A}$.

Heat transfer in solid

$$\rho_{\mathrm{s}}C_{\mathrm{ps}}\frac{\partial T_{\mathrm{s}}}{\partial t} = \nabla\cdot(\lambda_{\mathrm{s}}\nabla T_{\mathrm{s}}) + \sigma_{\mathrm{s}}E^2, \tag{18}$$

where T_{s}, ρ_{s}, C_{ps}, λ_{s} and σ_{s} are the temperature, the mass density, the specific heat, the thermal conductivity and the electric conductivity of the solid anode, respectively. Two kinds of anodes made by copper and tungsten with thorium oxide are investigated, since these two anodes are often used in arc experimental devices.[12,32] The specific heat, electrical conductivity and thermal conductivity of anode materials are taken from Ref. [33].

2.4. Boundary conditions

The boundary conditions used in the model are listed in Table 2. Zero gradients of electron temperature and species density are set at the cathode surface, inlet and outlet. Dirichlet boundary conditions of heavy-species temperature and solid temperature are set on the boundaries except the anode surface (GH). For the velocity boundary conditions, no slip conditions are set on solid walls. Normal inflow velocity is defined on inlet to keep the flow rate and $p = 1$ atm is set on the outlet. For the vector potential, zero gradient is given on electrode surfaces. The current density on boundary AB is set as a constant value with reference to Ref. [4], and on boundary BC it is set as the exponential distribution referring to Refs. [34,35]. The anode bottom is connected to ground. The ions boundary condition in species conservation equation is $-J_{\mathrm{iw,a}}$, and boundary conditions of neutral species are set as zero gradient on the anode.

Table 2. The boundary conditions used in the numerical model.

Boundary	Electron energy	Heavy-species and anode temperature	Current density	Velocity & pressure	Species	Vector potential
AB	$\boldsymbol{n}\cdot\nabla T_{\mathrm{e}} = 0$	$T_{\mathrm{h}} = 3500$ K	$j = j_{\mathrm{given}}$	$v = 0$	$\boldsymbol{n}\cdot\nabla\rho_{\mathrm{i}} = 0$	$\boldsymbol{n}\cdot\nabla A = 0$
BC	$\boldsymbol{n}\cdot\nabla T_{\mathrm{e}} = 0$	$T_{\mathrm{h}} = 3200\frac{(r-0.5)}{1.1} + 300$ K	$j = j_{\mathrm{given}}$	$v = 0$	$\boldsymbol{n}\cdot\nabla\rho_{\mathrm{i}} = 0$	$\boldsymbol{n}\cdot\nabla A = 0$
CD	$\boldsymbol{n}\cdot\nabla T_{\mathrm{e}} = 0$	$T_{\mathrm{h}} = 300$ K	$\boldsymbol{n}\cdot\boldsymbol{j} = 0$	$v =$ const.	$\boldsymbol{n}\cdot\nabla\rho_{\mathrm{i}} = 0$	$A = 0$
DH	$\boldsymbol{n}\cdot\nabla T_{\mathrm{e}} = 0$	$T_{\mathrm{h}} = 300$ K	$\boldsymbol{n}\cdot\boldsymbol{j} = 0$	$p = 1$ atm	$\boldsymbol{n}\cdot\nabla\rho_{\mathrm{i}} = 0$	$A = 0$
EH	–	$T_{\mathrm{s}} = 300$ K	$\boldsymbol{n}\cdot\boldsymbol{j} = 0$			
GH	$-q_{\mathrm{ew,a}}^{(\mathrm{pl})}$	$q_{\mathrm{w,a}} - q_{\mathrm{hw,a}}^{(\mathrm{pl})}$		$v = 0$	$\boldsymbol{n}\cdot\nabla\rho_{\mathrm{i}} = 0$ (for atom) $\boldsymbol{n}\cdot\nabla\rho_{i} = -J_{\mathrm{iw,a}}$ (for ions)	$\boldsymbol{n}\cdot\nabla A = 0$
EF	–	$T_{\mathrm{s}} = 300$ K	ground	–	–	–

The calculation domain includes the plasma flow affected region, pre-sheath and space charge sheath. In the two-temperature chemical non-equilibrium model, the pre-sheath, located in the near-anode region, is part of the plasma arc. Since the thickness of the space charge sheath is small, the space charge sheath can be treated as a zero-dimensional interface separating the plasma from the anode, and the appropriate boundary conditions are imposed to provide the sheath features.

In the anode region, the thermal emission current $j_{\mathrm{em,a}}$ is negligible due to the low temperature and the current density j consists of the current $j_{\mathrm{ew,a}}$ of the diffusing electrons reaching the anode and ion current $j_{\mathrm{iw,a}} = \sum_i J_{i\mathrm{w,a}} e$. The current density is given by

$$j = j_{\mathrm{ew,a}} - j_{\mathrm{iw,a}}. \tag{19}$$

The $J_{i\mathrm{w,a}} = \frac{n_i \cdot C_i}{4} \exp\left(-\frac{eU_{\mathrm{d,a}}}{kT_i}\right)$ represents the ion flux ($\mathrm{N_2^+}$, $\mathrm{N^+}$ and $\mathrm{N^{++}}$) coming to the interface from the plasma. n_i and C_i are respectively the ion number density and thermal velocity of species i, and $U_{\mathrm{d,a}}$ is the anode sheath voltage that is set as zero due to its small value.[22]

The heat flux on the anode surface is given as follows:

$$q_{\mathrm{w,a}} = q_{\mathrm{ew,a}}^{(\mathrm{pl})} + q_{\mathrm{hw,a}}^{(\mathrm{pl})} + q_{\mathrm{ec,a}} + q_{\mathrm{ir,a}} - q_{\mathrm{rad,a}}, \tag{20}$$

$$q_{\mathrm{ew,a}}^{(\mathrm{pl})} = \frac{j_{\mathrm{ew,a}}}{e}(2k_{\mathrm{B}}T_{\mathrm{e}} + eU_{\mathrm{d,a}}), \tag{21}$$

$$q_{\mathrm{hw,a}}^{(\mathrm{pl})} = -\lambda_{\mathrm{h}}\nabla T_{\mathrm{h}} + \sum_{i\neq e} h_i \boldsymbol{J}_i, \tag{22}$$

$$q_{\mathrm{ec,a}} = \frac{j}{e}A_{\mathrm{a}}, \tag{23}$$

$$q_{\mathrm{ir,a}} = \sum_i J_{i\mathrm{w,a}}^{(\mathrm{pl})} \varepsilon_i, \tag{24}$$

$$q_{\mathrm{rad,a}} = -\varepsilon\beta T^4, \tag{25}$$

where $q_{\mathrm{ew,a}}^{(\mathrm{pl})}$ and $q_{\mathrm{hw,a}}^{(\mathrm{pl})}$ represent the heat flux from the plasma electrons and heavy-species, respectively, which accounts for heat conduction and enthalpy transport. $q_{\mathrm{ec,a}}$ is the heat flux released by electron condensation and $q_{\mathrm{ir,a}}$ is the ion recombination heat flux. The work functions A_{a} of different anode materials are taken from Ref. [36]. $q_{\mathrm{rad,a}}$ is the radiation loss of the anode. In Eq. (25), ε is the surface emissivity and β is the Stefan–Boltzmann constant. In the calculation, the heavy-species energy equation and anode energy equation are solved simultaneously by considering the heat transfer at the interface. Considering the effect of anode sheath, the ions and electron energy fluxes are respectively set on the interface for the species and electron energy equations to obtain the reasonable parameters distributions. So the sheath layer is coupled to the calculation of the plasma arc by imposing the appropriate boundary conditions on the interface.

3. Results and discussion

3.1. Validation of the model

In order to validate our two-temperature chemical non-equilibrium model, the temperature distributions in plasma column are compared with the experimental measurement data of Haidar[12] and Murphy,[13] so the simulations are performed under the same working conditions as experimental measurements. The arc current is 200 A and the gas flow rate is set to 5 slpm. In the experiment the thoriated tungsten anode is adopted, which is cooled by direct contact with water and by conduction through the copper plate.[12] Figure 2 presents a comparison of our calculated temperature distribution with

the spectroscopic measurement data. The lines are our numerical results and the dots are the measurement data obtained by Fowler–Milne method. It is seen that the isotherms of 24000 K, 19000 K, 14000 K and 9000 K agree well with the experimental measurement data, except for small difference occurring in the arc fringe.

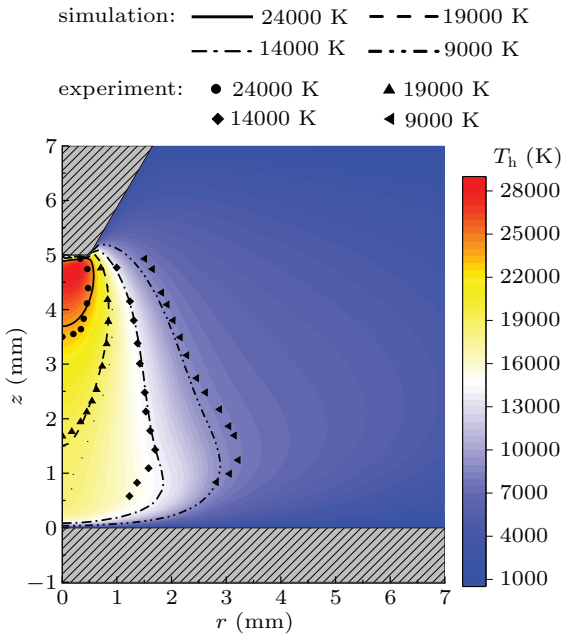


Fig. 2. Temperature distribution of nitrogen plasma at 200 A arc current, the lines are the calculated heavy-species temperature and the dots are the measurement data taken from Ref. [12].

Figure 3 presents the radial distributions of our calculated electron temperature and experimentally measured temperature at different arc current conditions. The calculated temperature distributions are in reasonable agreement with the experimental data in the arc current range from 100 A to 300 A. The maximum temperature has an obvious rise when the arc current increases from 100 A to 200 A, while the plasma temperature increases slowly in the arc currents of 200 A to 300 A. The variation trend of temperature distributions with arc current is consistent with the experimental results in Ref. [12].

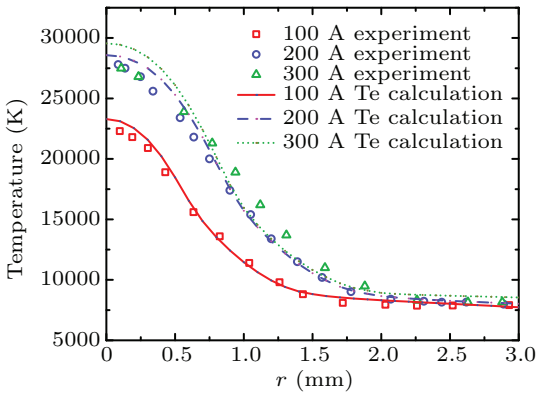


Fig. 3. Radial distribution of calculated temperature and experimentally measured data for different arc currents at an axial distance of 4.5 mm from anode surface.

Figure 4 further shows the comparison of electron and heavy-species temperatures of numerical model with the experimental data of Murphy[13] at different axial and radial positions. The symbols are experimental data measured by laser-scattering technique without the local thermal equilibrium assumption.[13] As shown in Fig. 4, the numerical results agree well with the experimental data in the arc center. However, in the arc fringe region, where the temperature is below 5000 K, the electron temperature and heavy-species temperature deviate from the measured data, especially for the temperature at the distances away from the anode. The discrepancy at the arc fringe may be caused by the chemical non-equilibrium processes. In general, these comparisons indicate that our present model can reasonably predict the temperature distributions of nitrogen arc.

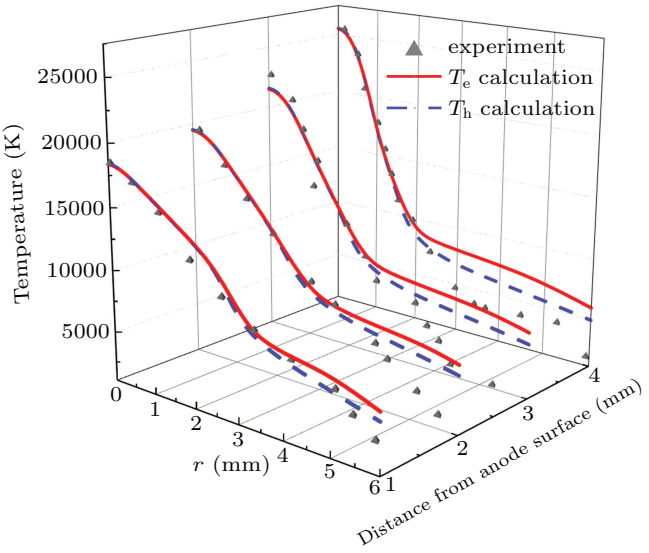


Fig. 4. Comparison of calculated electron and heavy-species temperatures with experimental data[13] at different axial and radial positions.

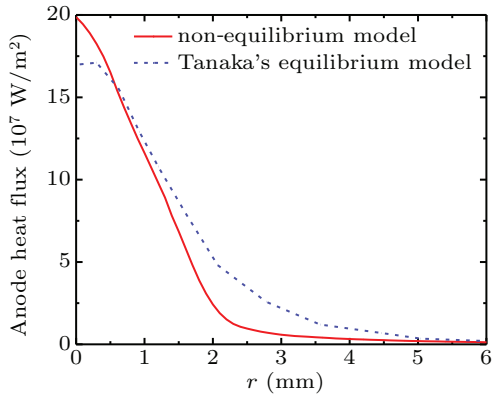


Fig. 5. Radial distribution of anode heat flux calculated by different numerical models at 150 A arc current.

Since we focus on the heat flux distribution on the anode surface, figure 5 exhibits the radial distribution of heat flux on copper anode surface at 150 A arc current. The anode heat flux calculated by Tanaka is based on the thermal and chemical

equilibrium model.[14] The total heat flux in Ref. [14] includes the heat conduction flux from plasmas and electron condensation heat. The anode heat flux in our model includes electron condensation heat, heat flux from heavy-species and electrons through conduction and enthalpy transport, ion recombination heat flux and radiation loss, which is calculated by thermal and chemical non-equilibrium model considering the collisionless space charge sheath. On the arc axis, the anode heat flux calculated by our non-equilibrium model is a little higher than that calculated by the equilibrium model. This may be due to the inclusion of more anode heat flux components in our model, such as heat released by ion recombination, which was ignored in Ref. [14]. In the arc fringe, there is a difference between the anode heat fluxes calculated by the two sets of numerical models. This discrepancy may be related to the effect of non-equilibrium characteristics.

3.2. Arc current effects on anode heat transfer

The influence of arc current on the heat transfer of thoriated tungsten anode is investigated in this section, in which the gas flow rate is fixed as 5 slpm. Figure 6 shows the temperature distribution of nitrogen arc plasma column at 100 A, 150 A and 200 A arc currents. The arc column shape is a typical bell-shape and the arc-anode attachment mode is diffuse. Enlargement of arc column is observed as the arc current increases from 100 A to 200 A. The maximum temperatures are respectively 25466 K, 26853 K and 28528 K for 100 A, 150 A and 200 A arc currents. Similarly, the temperature on the anode surface significantly rises with the arc current as shown in Fig. 7. The maximum temperatures on the anode surface are respectively 1350 K, 1900 K and 2450 K for the arc currents of 100 A, 150 A and 200 A. All temperatures are lower than the melting point of thoriated tungsten anode, which indicates that the non-ablating anode assumption is reasonable in these working conditions.

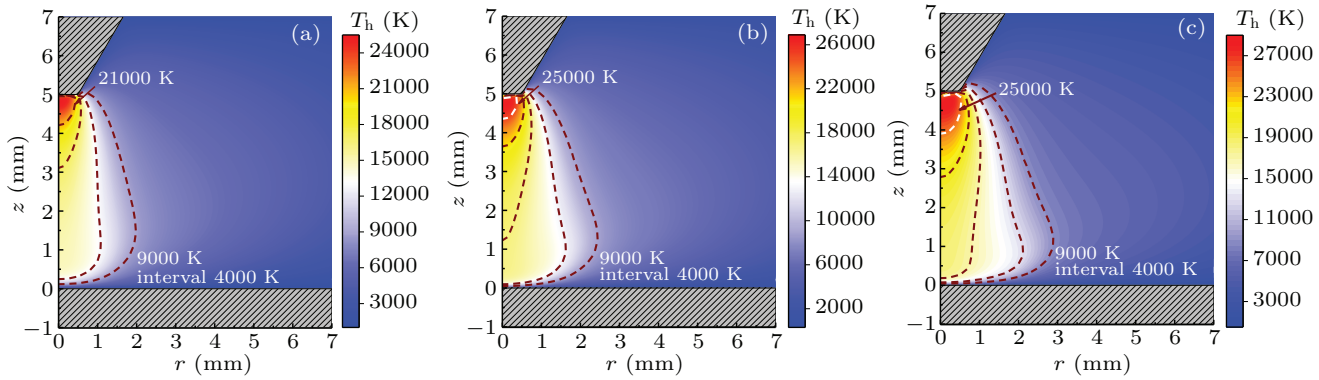


Fig. 6. Temperature distribution of nitrogen arc plasma at 100 A (a), 150 A (b), and 200 A (c) arc currents.

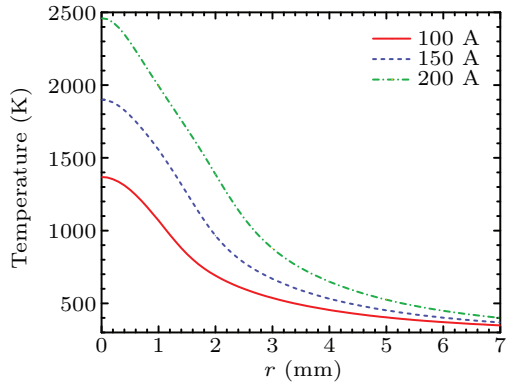


Fig. 7. Radial distribution of current density on thoriated tungsten anode surface at different arc currents.

Figure 8 shows the radial distribution of current density on thoriated tungsten anode surface at different arc currents. Contrary to the variation trend of temperature on the anode surface, the maximum current density slightly decreases as the arc current increases. The 'arc radius' is defined in order to clarify the changing trend of current density. It is defined as the radius that includes 90% of total arc current on the anode surface, which was also used in Ref. [37] to characterize the arc constriction. On the anode surface, the arc radii are respectively 1.76 mm, 1.90 mm and 2.29 mm for 100 A, 150 A and 200 A current conditions, which indicates that the arc anode attachment area becomes more diffuse with the increase of the arc current. This phenomenon is consistent with the enlargement of plasma arc column upon increasing the arc current. Hence, the decrease of the maximum current density on the arc axis is caused by the arc expansion.

In order to better understand the effect of arc current on the anode heat transfer, figure 9 respectively presents the radial distribution of different anode heat flux components on thoriated tungsten anode at different arc currents. As shown in this figure, the radiation loss ($q_{\mathrm{rad,a}}$) is very weak, which is negligible compared to the total heat flux. The heat flux from plasma electrons ($q_{\mathrm{ew,a}}^{(\mathrm{pl})}$), the electron condensation heat ($q_{\mathrm{ec,a}}$) and ion recombination term ($q_{\mathrm{ir,a}}$) decrease rapidly with the increase of the radial distance, which are mainly concentrated in the arc attachment region. The peak value of the total heat flux

increases from 1.0×10^8 W/m^2 to 1.9×10^8 W/m^2 as the arc current increases from 100 A to 200 A. It is seen from Fig. 9 that the maximum value of each heat flux component increases with the arc current except the maximum electron condensation heat. The maximum value of electron condensation heat decreases from 6×10^7 W/m^2 to 5×10^7 W/m^2, which is consistent with the variation of current density. Moreover, the maximum value of ion recombination term rapidly rises, even slightly exceeding the electron condensation heat on the symmetry axis at 200 A arc current. Figure 10 presents the radial distribution of the ratio of different heat flux components to the total heat flux in order to clarify the contribution of different heat flux components. As the arc current rises from 100 A to 200 A, the peak value of the ratio of $q_{\mathrm{ir,a}}$ increases from 3.0% to 28.3%, and its contribution is mainly concentrated in the region within 1 mm away from the arc axis. On the arc axis the ratios of $q_{\mathrm{ew,a}}^{(\mathrm{pl})}$ and $q_{\mathrm{hw,a}}^{(\mathrm{pl})}$ are basically unchanged with the arc current. The ratio of $q_{\mathrm{ec,a}}$ first rises, and then decreases as the radial distance increases. The ratio of $q_{\mathrm{hw,a}}^{(\mathrm{pl})}$ monotonically rises with the radial distance and is close to 100% in the arc fringe, which is the dominant contribution of heat transfer in the low temperature region. In general, the contributions of $q_{\mathrm{ew,a}}^{(\mathrm{pl})}$, $q_{\mathrm{ir,a}}$ and $q_{\mathrm{ec,a}}$ concentrate in the arc-anode attachment region, while the $q_{\mathrm{hw,a}}^{(\mathrm{pl})}$ plays a dominant contribution in the arc fringe.

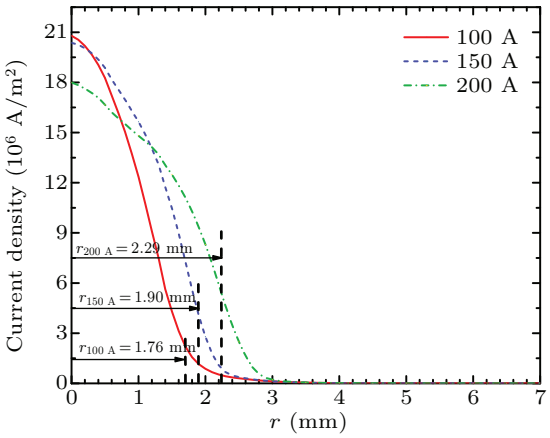


Fig. 8. Radial distribution of current density on thoriated tungsten anode surface at different arc currents.

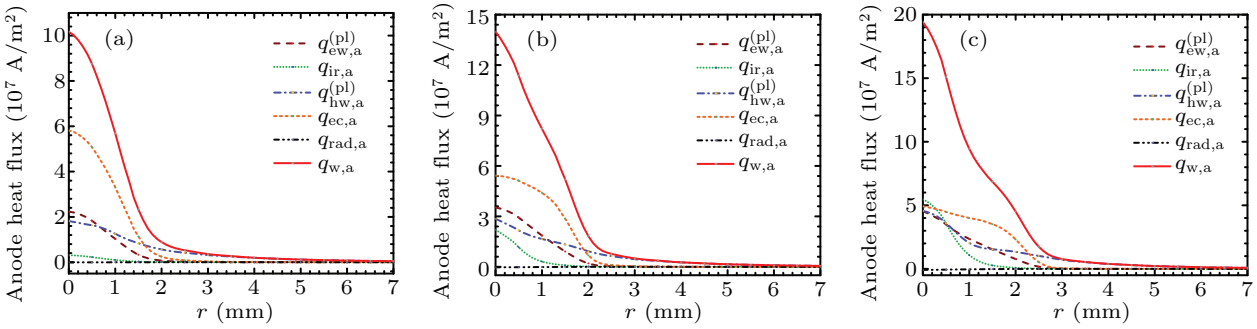


Fig. 9. Radial distribution of anode heat flux on thoriated tungsten anode surface at arc currents of 100 A (a), 150 A (b), and 200 A (c).

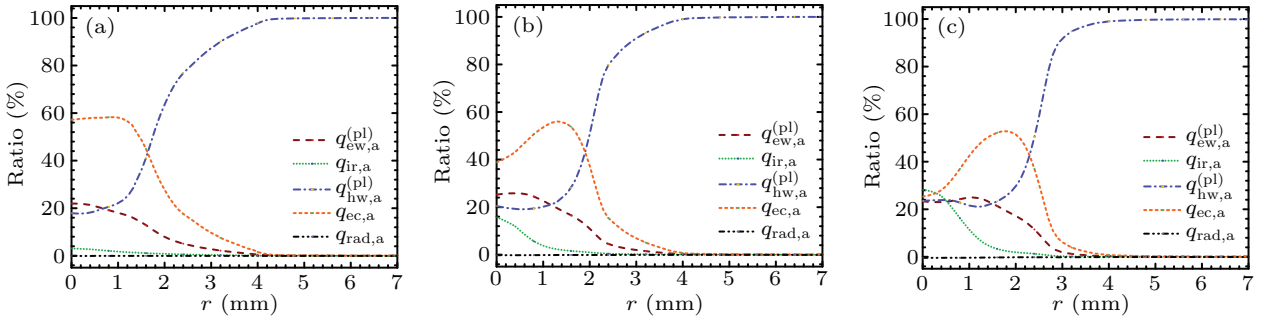


Fig. 10. Radial distribution of the ratio of different heat flux components on thoriated tungsten anode surface at arc currents of 100 A (a), 150 A (b), and 200 A (c).

Table 3 gives the ratio of power transferred to anode through each heat flux component. The power ratio of different heat flux components is obtained as follows: first integrate each heat flux component ($q_{\mathrm{ew,a}}^{(\mathrm{pl})}$, $q_{\mathrm{ir,a}}$, $q_{\mathrm{hw,a}}^{(\mathrm{pl})}$, $q_{\mathrm{ec,a}}$, $q_{\mathrm{rad,a}}$) on the anode surface to obtain the corresponding power component ($Q_{\mathrm{ew,a}}^{(\mathrm{pl})}$, $Q_{\mathrm{ir,a}}$, $Q_{\mathrm{hw,a}}^{(\mathrm{pl})}$, $Q_{\mathrm{ec,a}}$, $Q_{\mathrm{rad,a}}$), then divide the power of different heat flux by the total power $Q_{\mathrm{w,a}}$, i.e., the integral of $q_{\mathrm{w,a}}$, to get the power ratio. The power transferred to the thoriated tungsten anode in the descending order is $Q_{\mathrm{hw,a}}^{(\mathrm{pl})}$, $Q_{\mathrm{ec,a}}$, $Q_{\mathrm{ew,a}}^{(\mathrm{pl})}$ and $Q_{\mathrm{ir,a}}$. Moreover, the order of different heat flux components will not change as the current increases from 100 A to 200 A. It is seen that more than 75% of the power is transferred by $Q_{\mathrm{hw,a}}^{(\mathrm{pl})}$ and $Q_{\mathrm{ec,a}}$. From the radial distributions of different heat fluxes shown in Figs. 9 and 10, it may be inferred that the power is mainly transferred by $Q_{\mathrm{ec,a}}$ in the plasma column and by $Q_{\mathrm{hw,a}}^{(\mathrm{pl})}$ in the arc fringe. Although the ratio of $q_{\mathrm{ir,a}}$ exceeds 25% on the arc axis in Fig. 10(c), the contribution of its power is lower than 7% at 200 A arc current due to the steep gradient

in the radial direction.

Table 3. Radial distribution of temperature on thoriated tungsten anode surface at different arc currents.

Components	Power ratio		
	100 A	150 A	200 A
$Q_{ew,a}^{(pl)}$	11.52%	14.50%	15.71%
$Q_{ir,a}$	1.23%	3.16%	6.80%
$Q_{hw,a}^{(pl)}$	51.40%	46.58%	45.09%
$Q_{ec,a}$	35.92%	35.89%	32.65%
$Q_{rad,a}$	–0.07%	–0.13%	–0.25%

3.3. Material effects on anode heat transfer

Reasonable selection of electrode materials is of importance to extend the lifetime of arc device. Therefore, the effects of materials on the anode heat transfer are investigated in this section. The tungsten doped with thorium is often adopted as the anode material of nitrogen arc device.[12,13] On the other hand, the copper anode is also widely applied in the transferred and non-transferred arc devices.[32] Thus in this study the copper anode and thoriated tungsten anode are selected to investigate the material effects on anode heat transfer.

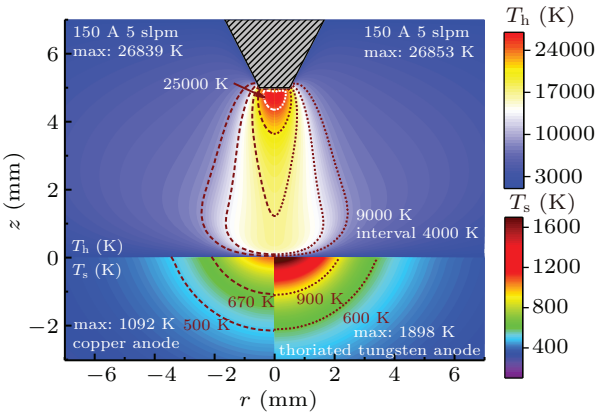


Fig. 11. Temperature distributions of nitrogen arc at 150 A arc current for different anode materials.

Figure 11 presents the temperature distributions of nitrogen plasma at 150 A arc current for different anode materials. It can be seen that the temperature differences in plasma arc column are negligible for the copper anode and thoriated tungsten anode. Both the arc profile and the maximum temperature are almost the same for the copper anode and thoriated tungsten anode. Although there is almost no difference in the temperature of arc column, the temperature in the anode region is obviously different. The maximum temperature is 1092 K on the copper anode surface, which is about 800 K lower than the maximum temperature on thoriated tungsten anode surface. Moreover, the temperature gradient is steeper in the thoriated tungsten anode due to lower thermal conductivity, leading to a higher maximum temperature in the thoriated tungsten anode. Therefore, these results indicate that anode materials have a significant influence on temperature distribution in the anode region, while the temperature of plasma column is hardly affected by anode materials in the case of non-ablating anode.

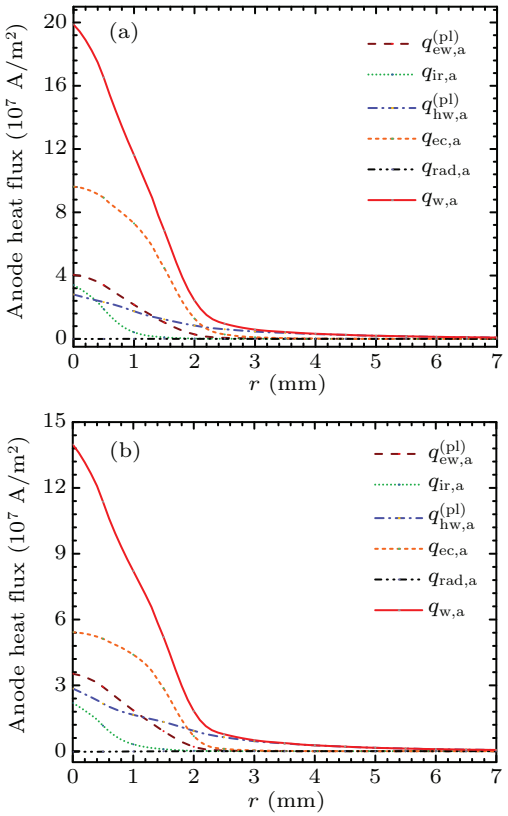


Fig. 12. Radial distribution of heat flux on copper anode surface (a) and thoriated tungsten anode surface (b) at 150 A arc current.

Figure 12 describes the radial distribution of different heat flux components on copper anode and thoriated tungsten anode. As discussed above, the radiation loss ($q_{rad,a}$) is still negligible to the total anode heat flux ($q_{w,a}$). The peak value of $q_{w,a}$ on copper anode is 1.96×10^8 W/m^2, which is higher than the maximum heat flux of 1.38×10^8 W/m^2 on thoriated tungsten anode. The difference in maximum heat flux is mainly caused by $q_{ec,a}$. From the above temperature analysis, it is found that the maximum temperature on copper anode surface is lower than that on thoriated tungsten anode surface, while higher heat flux is transferred from plasma to copper anode. This indicates that the heat flux from nitrogen arc spreads more easily in the copper anode due to its high thermal conductivity. As seen from the power ratio in Table 4, the power of each component transferred to the copper anode in descending order is $Q_{ec,a}$, $Q_{hw,a}^{(pl)}$, $Q_{ew,a}^{(pl)}$ and $Q_{ir,a}$. More than 80% of the power is transferred to copper anode by $Q_{ec,a}$ and $Q_{hw,a}^{(pl)}$. Compared with the thoriated tungsten anode, $Q_{ec,a}$ instead of $Q_{hw,a}^{(pl)}$ becomes the first contribution of the power transferred from nitrogen arc. This is consistent with the variation tendency of argon arc with copper anode in Ref. [38]. The comparison indicates that higher heat flux on anode may not produce higher anode temperature. The choice of anode material is crucial, and it is inferred that the materials with high melting point and high thermal conductivity are more suitable as the anode of arc device to prolong the anode lifetime. On the contrary, the arc process is suitable for processing materials with low thermal

conductivity, high work function and low melting point.

Table 4. The ratio of power transferred to the anode through each heat flux component at 150 A arc current.

Components	Power ratio	
	Copper anode	Thoriated tungsten anode
$Q_{ew,a}^{(pl)}$	12.78%	14.50%
$Q_{ir,a}$	3.40%	3.16%
$Q_{hw,a}^{(pl)}$	38.72%	46.58%
$Q_{ec,a}$	45.13%	35.89%
$Q_{rad,a}$	–0.03%	–0.13%

4. Conclusions

The two-temperature chemical non-equilibrium model is adopted to investigate the anode heat transfer of nitrogen arc in this paper. The interactions of plasma arc with the anode are considered in detail by including the collisionless space charge sheath. The electron and heavy-species temperature distributions are compared with the experimental data to validate our model. Moreover, the total anode heat flux calculated by our non-equilibrium model is compared with that of equilibrium model of Tanaka. Then we use the two-temperature chemical non-equilibrium model to study the effects of different arc currents and anode materials on the anode heat transfer.

The results indicate that the arc current affects the temperature and heat flux distribution of anode region by changing the plasma characteristics distributions in the arc column. As the arc current increases from 100 A to 200 A, the plasma arc column enlarges, resulting in the more diffuse arc anode attachment region. Therefore, the maximum electron condensation heat flux decreases with the increase of arc current, while the maximum heat fluxes from plasma electrons and heavy-species and ion recombination heat increase. It is found that the electron condensation heat flux, the heat flux from plasma electrons and ion recombination heat flux are mainly concentrated in the high current density region. The heat flux from heavy-species decays slowly in the radial direction, becoming the main heat flux component in the arc fringe. The power transferred to the anode by each heat flux component is obtained. The contribution of each heat flux component to power transferred to anode changes slightly in the current range from 100 A to 200 A. The heat flux from plasma heavy-species and the electron condensation heat are the first and second contributions to power transferred to the thoriated tungsten anode.

The anode material hardly affects the temperature distribution of plasma arc column, while it has a significant effect on the temperature and heat flux distributions in the anode region. The total heat flux on copper anode is higher than that on thoriated tungsten anode, and this difference is mainly caused by electron condensation heat. However, the maximum temperature on copper anode is lower than that on thoriated tungsten anode. This phenomenon is caused by a steeper temperature gradient in the thoriated tungsten anode region due to the lower heat conductivity. For the copper anode, the maximum contribution to power transferred to anode is electron condensation heat, which is different from that of thoriated tungsten anode. The electron condensation heat instead of heat flux from plasma heavy-species makes the largest contribution to power transferred to anode due to the high work function of copper.

References

[1] Murphy A B 2010 *J. Phys. D: Appl. Phys.* **43** 434001
[2] Murphy A B 2015 *Plasma Chem. Plasma Process* **35** 471
[3] Murphy A B 2018 *Plasma Sources Sci. Technol.* **27** 63001
[4] Mckelliget J and Szekely J 1986 *Metall. Mater. Trans. A* **17** 1139
[5] Zhao P, Ni G H, Meng Y D and Masaaki N 2013 *Chin. Phys. B* **22** 064701
[6] Lin Q F, Zhao Y J, Duan W X, Ni G H, Jin X Y, Sui S Y, Xie H B and Meng Y D 2020 *Chin. Phys. B* **29** 125201
[7] Xu B, Jiang F, Chen S J, Tanaka M, Tashiro S and Anh N V 2018 *Chin. Phys. B* **27** 034701
[8] Lago F, Gonzalez J, Freton P and Gleizes A 2004 *J. Phys. D: Appl. Phys.* **37** 883
[9] Baeva M, Kozakov R, Gorchakov S and Uhrlandt 2012 *Plasma Sources Sci. Technol.* **21** 055027
[10] Lu S P, Dong W C, Li D Z and Li Y Y 2009 *Comput. Mater. Sci.* **45** 327
[11] Sakura N, Yoshida M and Tanaka M 2019 *J. Phys. D: Appl. Phys.* **52** 404002
[12] Haidar J and Farmer A J D 1993 *J. Phys. D: Appl. Phys.* **26** 1224
[13] Murphy A B 1994 *J. Phys. D: Appl. Phys.* **27** 1492
[14] Tanaka M, Tashiro S, Satoh T, Murphy A B and Lowke J J 2008 *Sci. Technol. Weld Join.* **13** 225
[15] Chen X and Li H P 2001 *Int. J. Heat Mass Transf.* **44** 2541
[16] Li H P, Ostrikov K K and Sun W 2018 *Phys. Rep.* **770** 1
[17] Guo H, Zhang X, Chen J, Li H P and Ostrikov K 2018 *Sci. Rep.* **8** 4783
[18] Li H P annd Benilov M S 2007 *J. Phys. D: Appl. Phys.* **40** 2010
[19] Nemchinsky V A 2005 *J. Phys. D: Appl. Phys.* **38** 4082
[20] Wang H X, Zhu T, Sun S R, Liu G and Murphy A B 2020 *J. Phys. D: Appl. Phys.* **53** 505205
[21] Benilov M S, Almeida N A, Baeva M, Cunha M D and Benilova L G 2016 *J. Phys. D: Appl. Phys.* **49** 215201
[22] Baeva M, Benilov M S, Almeida N A and Urhlandt D 2016 *J. Phys. D: Appl. Phys.* **49** 245205
[23] Tanaka Y and Sakuta T 2002 *J. Phys. D: Appl. Phys.* **35** 468
[24] Tanaka Y 2004 *J. Phys. D: Appl. Phys.* **37** 1190
[25] Dunn M G and Lordi J A 1969 *AIAA J.* **8** 339
[26] Dutuit O, Carrasco N, Thissen R, Vuitton V, Alcaraz C, Pernot P, Balucani N, Casavecchia P, Canosa A, Picard S L, Loison J C, Herman Z, ZabKA J, Ascenzi D, Tosi P, Franceschi P, Prince S D and Lavvas P 2013 *Astrophys. J. Suppl. Ser.* **204** 20
[27] Bird R B, Stewart W E and Lightfoot E N 2002 *Transport phenomena*, 2nd edn. (New York: John Wiley & Sons, Inc.) p. 2627
[28] Colombo V, Ghedini E and Sanibondi P. 2008 *Prog. Nucl. Energy* **50** 921
[29] Devoto R S 1973 *Phys. Fluids* **16** 616
[30] Ramshaw J D and Chang C H 1991 *Plasma Chem. Plasma Process* **11** 395
[31] Fridman A, Cho Y I, Greene G A and Bar-cohen A 2007 *Transport phenomena in plasma: advances in heat transfer*. (Waltham: Academic Press, Elsevier) p. 391
[32] Zhou X 2017 *Experimental study on dispersing behaviour of direct-current arc in anode chamber* [Master's dissertation]. (Beijing: The University of Chinese-Academy of Sciences) (in Chinese)
[33] Konishi K, Shigeta M, Tanaka M, Murata A, Murata T and Murphy A B 2017 *Weld World* **61** 197
[34] Hsu K C 1982 *A self-consistent model for the high intensity free-burning argon arc* [Ph. D. dissertation]. (Minneapolis: University of Minnesota)
[35] Hsu K C, Etemadi K and Pfender E 1983 *J. Appl. Phys.* **54** 1293
[36] Baeva M 2017 *Plasma Chem. Plasma Process* **37** 341
[37] Tanaka M and Lowke J J 2007 *J. Phys. D: Appl. Phys.* **40** 1
[38] Jenista J, Heberlein J V R and Pfender E 1997 *IEEE Trans. Plasma Sci.* **25** 883